Three-Phase Inverter Fed Adjustable Field IPMSM Drive Utilizing Zero-Sequence Current

Kiyohiro Iwama, *Student Member, IEEE*, and Toshihiko Noguchi, *Senior Member, IEEE*

***Abstract*—This article proposes a three-phase four-wire inverter drive system for an adjustable field interior permanent magnet synchronous motor utilizing magnetic saturation. The magnetic saturation is regarded as a phenomenon of a decrease in permeability depending on an extra magnetic field. In the proposed motor, the number of flux linkage can be controlled by modulating the permeability of magnetic leakage paths in the rotor. However, the proposed adjustable field method requires an additional magnetomotive force (m.m.f.) to control the permeability. Therefore, a zero-sequence current i_z fed by the three-phase four-wire inverter is utilized as the additional m.m.f. source. Thereby, the field control can be achieved with a simple three-phase inverter without sacrificing the number of switching devices compared with conventional motor drives. In the article, the control algorithm of the three-phase four-wire inverter is discussed, and its usefulness is verified by comparing the proposed drive system with other methods or systems.**

***Index Terms*—Adjustable field, magnetic saturation, three-phase four-wire inverter, zero-sequence current.**

I. Introduction

DRIVING range of a permanent magnet synchronous motor (PMSM) is limited due to a constant PM flux. Conventionally, a field weakening control has been used [1]–[5]. However, the copper loss caused by a negative d-axis current i_d for the field weakening control becomes significant as demand for higher speed increases.

Therefore, adjustable field PMSMs have intensively been researched [6]–[13]. In [6] and [7], a consequent pole type adjustable field PMSM is proposed. The adjustable field PMSM can control the magnetic field using a static magnetic field generated by a dc field current fed by a dc–dc converter. Another adjustable field IPMSM introduced in [8]–[10] can realize an expansive driving range, including both high-speed low-torque and low-speed high-torque, using de- and remagnetization of the PM. There is another adjustable field method utilizing motor harmonics, such as space and time harmonics. The adjustable field method described in [11] utilizes the space harmonics as magnetic field energy by using special windings and rectifier circuits in the rotor. Another adjustable field method switches over the winding configurations as reported in [12]. The adjustable field method can change the number of flux linkage discretely by switching over the winding configurations such as a three-phase or a six-phase drive.

However, the drive systems of the conventional adjustable field PMSMs require additional circuits and tend to be bulky in size. Iwama and Noguchi [13] investigated an adjustable field method focusing on a magnetic saturation phenomenon. A prototype motor with the proposed adjustable field method has a wide controllable range of the magnetic field, but the additional current (modulation current i_m) is needed for the magnetic field control. Therefore, this article proposes a drive system to achieve magnetic field control without additional circuits and switching devices. The proposed drive is based on a three-phase four-wire inverter, and in addition to i_d and i_q, a 0-axis current i_0 for the adjustable field can be controlled.

Fig. 1 shows the research position. The proposed drive system using the three-phase four-wire inverter is introduced while comparing it with conventional adjustable field PMSM drive systems in Section III. In addition, the losses caused by the proposed adjustable field method with the trapezoidal wave i_0 are compared with the losses generated by the field weakening control in Section IV-A. Moreover, the proposed drive system is compared with drive systems using an additional dc power supply or single-phase inverter in terms of the system volume and the operation characteristics in Section VI. The following advantages of the proposed adjustable field method and system are revealed through these comparisons:

1) The magnetic field can be controlled with a smaller number of switching devices and wirings than the conventional adjustable field PMSM drive systems.
2) A high-speed operation can be achieved with less current norm, voltage harmonics, and iron loss than field weakening control.
3) The same torque as when the trapezoidal wave i_m is supplied from the additional single-phase inverter can be delivered, even though the additional circuit is not used.

Manuscript received 23 November 2021; revised 18 February 2022 and 22 March 2022; accepted 26 March 2022. Date of publication 12 April 2022; date of current version 5 October 2022. This work was supported by JSPS KAKENHI under Grant JP21K04022. *(Corresponding author: Kiyohiro Iwama.)*

The authors are with the Department of Environment and Energy System, Shizuoka University, Hamamatsu 432-8561, Japan (e-mail: iwama.kiyohiro.14@shizuoka.ac.jp; noguchi.toshihiko@shizuoka.ac.jp).

Color versions of one or more figures in this article are available at https://doi.org/10.1109/TIE.2022.3165300.

Digital Object Identifier 10.1109/TIE.2022.3165300

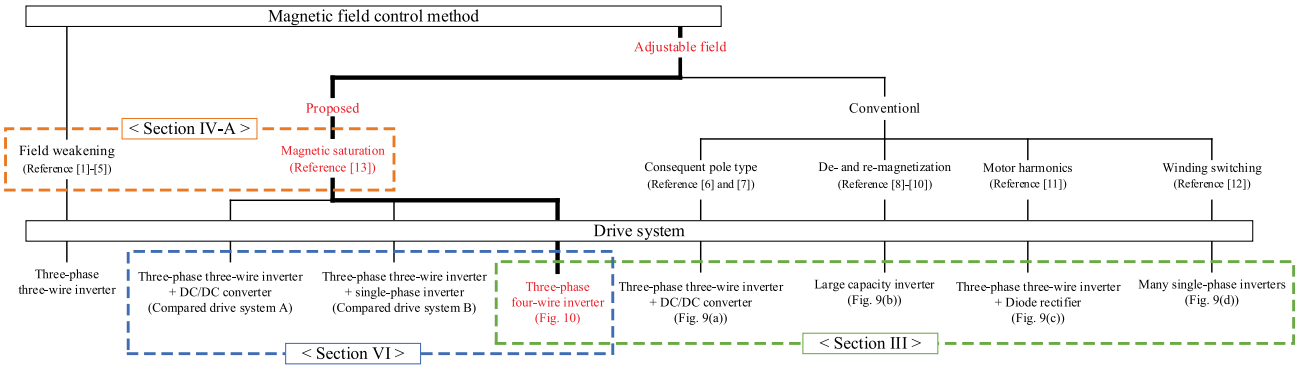

Fig. 1. Research position of proposed adjustable field method and drive system.

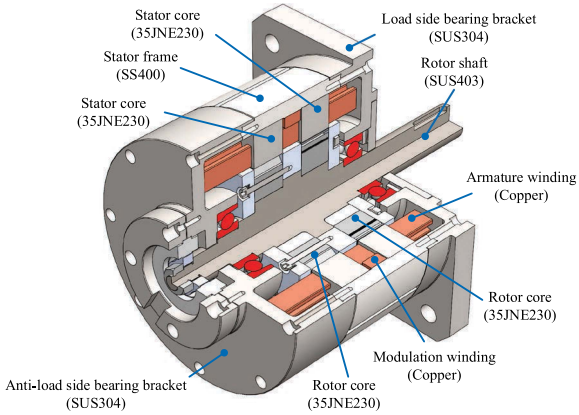

Fig. 2. Configuration of prototype motor.

TABLE I
SPECIFICATIONS OF PROTOTYPE MOTOR

Number of poles and slots	8 poles, 48 slots
Number of armature winding turns	6 turns/slot
Number of modulation winding turns	140 turns
Stator diameter	ϕ148 mm
Rotor diameter	ϕ 96.6 mm
Stack length	63 mm

II. Essential Characteristics of Prototype Motor

A. Specifications of Prototype Motor

As described previously, the proposed adjustable field method utilizes magnetic saturation. The modulation flux to control magnetic saturation (permeability) in the rotor iron core and the resultant magnetic field is generated by the modulation current i_m. Figs. 2, 3, and Table I show a development view, photographs, and specifications of the prototype motor, respectively. As shown in Figs. 2 and 3, the stator core and the rotor core are split into two parts, and the modulation winding is inserted between the split two stator cores. The stator frame and the rotor shaft of the prototype motor are made of magnetic materials such as SS400 and SUS403. Therefore, the modulation flux can penetrate the stator frame and the rotor shaft. In this article, the zero-sequence current i_z is utilized as the i_m. In this case, the i_z flows into three-phase armature windings, and the copper loss of the armature windings can increase due to the i_z. To

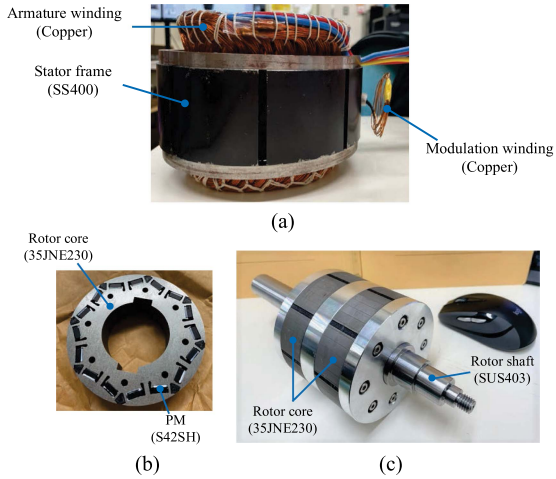

Fig. 3. Photographs of prototype motor. (a) Stator. (b) Rotor core. (c) Rotor.

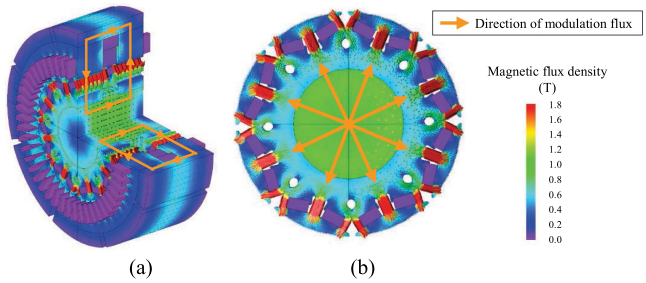

Fig. 4. Modulation flux with i_m of 5 A_{dc}. (a) 3-D magnetic path for modulation flux. (b) Radial modulation flux in rotor.

reduce the copper loss, the number of modulation winding turns is set to 140 turns, which is much larger than the number of armature winding turns. The design makes it possible to obtain appropriate m.m.f. with low i_z and reduce the current flowing through the armature winding.

Fig. 4 shows a vector plot of the modulation flux analyzed by JMAG-Designer ver. 20.1. It can be confirmed from Fig. 4 that the modulation flux penetrates in the radial direction in the rotor utilizing the three-dimensional magnetic path composed of the rotor shaft and the stator frame. Fig. 5 shows the magnetic flux density distribution in the air gap of one pair of the rotor and

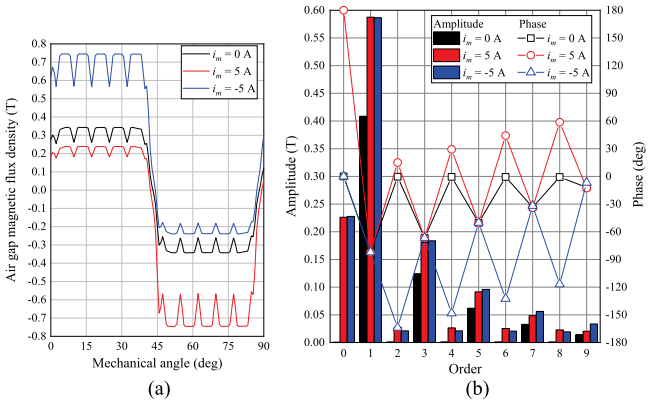

Fig. 5. Gap magnetic flux density. (a) Waveforms. (b) FFT results.

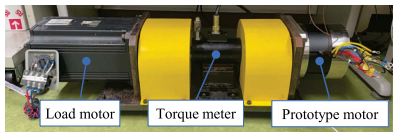

Fig. 6. Photograph of motor test rig.

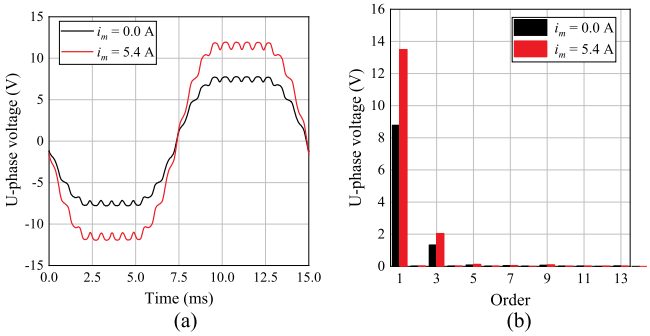

Fig. 7. Experimental results of no-load e.m.f. with i_m of 0 A_{dc} or 5.4 A_{dc}. (a) Waveforms. (b) FFT results.

the stator cores. The air gap of the other pair has inversely the same magnetic flux density distribution as the first pair, as shown in Fig. 5. The fundamental component of the air gap magnetic flux density distribution can be adjusted by the i_m. In addition, the amount of the fundamental component is not affected by the i_m polarity. The radial modulation flux strengthens one PM pole (e.g., N-pole) and weakens the other PM pole (e.g., S-pole). Therefore, even-order harmonic components are generated in the air gap magnetic flux density distribution. However, the phase difference between the even-order components of the two air gap magnetic flux densities is 180°. Therefore, these harmonics are canceled with each other and do not affect the e.m.f. and the output.

B. No-Load Characteristic

Fig. 6 shows the photograph of motor test rig. The rotating speed is controlled by the load motor. Fig. 7 shows experimental results of the no-load e.m.f. at the rotating speed N of 1000 r/min when the i_m of 0 A_{dc} or 5.4 A_{dc} is given to the modulation winding. As shown in the figure, the fundamental component of

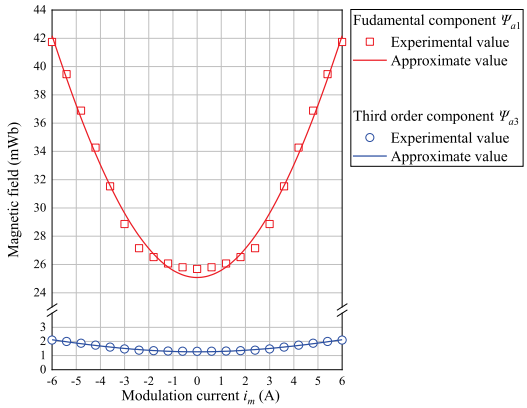

Fig. 8. Relationship between modulation current and magnetic field.

the no-load e.m.f. increases from 8.78 V_{amp} to 13.5 V_{amp} by supplying the i_m of 5.4 A_{dc}. In addition, harmonics other than the third order are negligibly small. Fig. 8 shows a relationship between the i_m and the magnetic field Ψ_{a1} and Ψ_{a3}, where the Ψ_{a1} and the Ψ_{a3} are obtained by converting the fundamental and the third order components of the no-load interlinkage flux from the three-phase reference frame to the 0dq reference frame, respectively. As shown in Fig. 8, the Ψ_{a1} and the Ψ_{a3} do not depend on the i_m polarity and can be controlled by the absolute value of the i_m. The Ψ_{a1} and the Ψ_{a3} can be approximated with polynomials of the i_m as follows:

$$\Psi_{a1}(i_m) = -1.15 \times 10^{-3}|i_m|^4 + 0.52|i_m|^2 + 25.1 \text{ (mWb) and} \quad (1)$$

$$\Psi_{a3}(i_m) = -9.45 \times 10^{-5}|i_m|^4 + 2.71 \times 10^{-2}|i_m|^2 + 1.27 \text{ (mWb).} \quad (2)$$

III. Drive Systems for Adjustable Field PMSM

A. Conventional Adjustable Field PMSM Drive Systems

Fig. 9 shows the adjustable field PMSM drives proposed so far. The drive system shown in Fig. 9(a) is based on an adjustable field method controlling the air gap magnetic flux density of a consequent pole PM motor [6], [7]. The drive system uses a dc–dc converter to supply the dc field current. Therefore, additional switching devices are required for the dc–dc converter, and the power losses consumed in the dc–dc converter deteriorate the whole system efficiency [14]–[16]. Fig. 9(b) shows another drive system for an adjustable field IPMSM utilizing de- and remagnetization of the PM mounted on the rotor [8]–[10]. In this method, the power electronics tend to be significant because the inverter needs to supply a high current of more than three times the motor-rated current for the de- and remagnetization of the PM. Fig. 9(c) shows another adjustable field PMSM drive utilizing the motor space harmonics [8]. The adjustable field method utilizes the space harmonics as a magnetic field energy source by rectifying the harmonics in the rotor. The

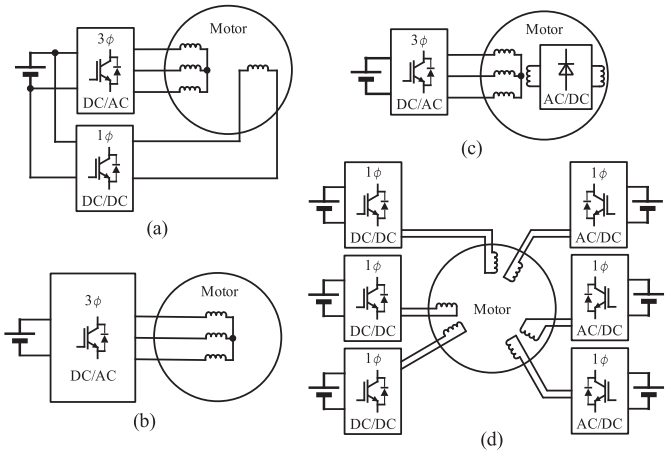

Fig. 9. Conventional adjustable field PMSM drives. (a) Method using dc–dc converter. (b) Method using de- and remagnetization of PM. (c) Method using space and/or time harmonics. (d) Method switching winding configurations.

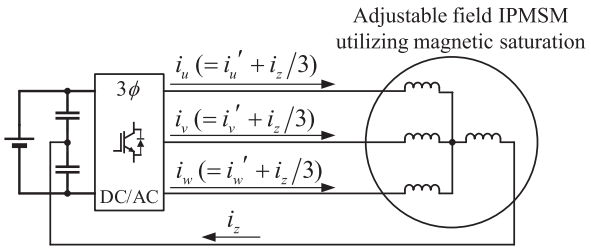

Fig. 10. Proposed adjustable field IPMSM drive.

rectifier circuit's switching and conduction losses degrade system efficiency [17]. Furthermore, this adjustable field method cannot control the magnetic field actively because the amount of the magnetic field passively depends on the rotating speed, according to Faraday's law. Fig. 9(d) shows an adjustable field IPMSM drive, which switches over the winding configurations [12]. The adjustable field system has six windings per pole pair and uses a single-phase inverter for each winding. In addition, bidirectional switching devices are indispensable for the connection and disconnection of the winding network. Therefore, the drive circuit must have excessively many switching devices, and the efficiency of the whole system tends to be worse than that of a conventional PMSM drive [18]–[21].

As described previously, the conventional adjustable field PMSM drives tend to be bulkier and more complicated than a typical PMSM drive.

B. Proposed Adjustable Field IPMSM Drive Systems

Fig. 10 shows a proposed adjustable field IPMSM drive utilizing magnetic saturation. The midpoint of the dc-bus is made by dividing the dc-bus voltage $V_{\rm dc}$ using the two series smoothing capacitors, and the modulation winding is connected between the midpoint of the $V_{\rm dc}$ and the motor neutral point. In this way, the electrical current path for the zero-sequence current $i_{\rm z}$ is made. The component $i_{\rm z}$ is evenly superimposed on the line currents i_u, i_v, and i_w as

$$\boldsymbol{i}_{uvw} = \begin{bmatrix} i_u \\ i_v \\ i_u \end{bmatrix} = \begin{bmatrix} i_u{}' + i_z/3 \\ i_v{}' + i_z/3 \\ i_u{}' + i_z/3 \end{bmatrix} \tag{3}$$

where $\boldsymbol{i}_{uvw}$ is an armature current vector on the three-phase reference frame, and $i_u{}'$, $i_v{}'$, and $i_w{}'$ are the three-phase balanced components of the line currents. In addition, the i_z is an in-phase component of the line currents on the three-phase reference frame. The conversion matrix $\boldsymbol{C}$ to convert from the three-phase reference frame to the $0dq$ reference frame is expressed as

$$\boldsymbol{C} = \sqrt{\frac{2}{3}} \begin{bmatrix} 1/\sqrt{2} & 1/\sqrt{2} & 1/\sqrt{2} \\ \cos\theta & \cos(\theta - 2\pi/3) & \cos(\theta + 2\pi/3) \\ -\sin\theta & -\sin(\theta - 2\pi/3) & -\sin(\theta + 2\pi/3) \end{bmatrix} \tag{4}$$

where θ is a spatial electrical angle. By using the $\boldsymbol{C}$, the $\boldsymbol{i}_{uvw}$ can be converted as where $\boldsymbol{i}_{0\,dq}$ is a current vector on the $0dq$ reference frame. It can be seen from (5) shown at the bottom of the next page, that the in-phase component i_z does not interfere with the i_d and the i_q, and the three-phase balanced components $i_u{}'$, $i_v{}'$, and $i_w{}'$ can be controlled without the influence of the i_0. Therefore, the i_0 can be used as the additional m.m.f. source for the field control independently of the conventional i_d and i_q control. When the i_0 is used as the i_m, the relationship between the i_0 and the i_m is expressed as

$$i_0 = i_z \Big/ \sqrt{3} = i_m \Big/ \sqrt{3}. \tag{6}$$

The voltage equation of the prototype motor is expressed as, (7) shown at the bottom of the next page, where $\boldsymbol{v}_{uvw}$ is a voltage vector on the three-phase reference frame, R_a is an armature winding resistance, p is a differential operator, $\boldsymbol{L}_{uvw}$ is an inductance matrix on the three-phase reference frame, Ψ_{uvw} is an interlinkage flux vector on the three-phase reference frame, $\boldsymbol{v}_z$ is a voltage at the motor neutral point, v_u, v_v, and v_w are phase voltages, L_u, L_v, and L_w are self-inductances of the three-phase windings, M_{uv}, M_{vw}, and M_{wu} are mutual inductances among the three-phase windings, $\Psi_{f1}(i_m)$ is the amplitude of the fundamental component of the no-load flux linkage, $\Psi_{f3}(i_m)$ is the amplitude of the third-order component of the no-load flux linkage, ω is an electrical angular speed, R_z is a modulation winding resistance, and L_z is an inductance of the modulation winding [22]. By using the $\boldsymbol{C}$, the $\boldsymbol{v}_{uvw}$ can be converted as

$$\mathbf{v}_{0dq} = \mathbf{C}\mathbf{v}_{uvw}$$

$$\begin{bmatrix} v_0 \\ v_d \\ v_q \end{bmatrix} = \begin{bmatrix} R_a + 3R_z + \mathrm{p}3L_z & 0 & 0 \\ 0 & R_a + \mathrm{p}L_d & -\omega L_q \\ 0 & \omega L_d & R_a + \mathrm{p}L_q \end{bmatrix} \begin{bmatrix} i_0 \\ i_d \\ i_q \end{bmatrix} + \begin{bmatrix} -3\omega\Psi_{a3}(i_m)\sin 3\omega t \\ 0 \\ \omega\Psi_{a1}(i_m) \end{bmatrix} \tag{8}$$

where $\boldsymbol{v}_{0\,dq}$ is a voltage vector on the $0dq$ reference frame, v_0, v_d, and v_q are the voltages on the $0dq$ reference frame, and L_d and L_q are the inductance on the $0dq$ reference frame. As described

previously, $\Psi_{a1}(i_m)$ and $\Psi_{a3}(i_m)$ can be expressed as (1) and (2), respectively.

It can be seen from (8) that the i_0 can be controlled using the v_0, which is a common-mode voltage. It means that the magnetic field can also be adjusted actively and continuously by the i_0. However, the dc i_0 can not apply due to the voltage imbalance of the smoothing capacitors. Hence, the trapezoidal wave i_0 is used in this article. The influence of the L_z on the voltage utilization can be suppressed by setting the i_0 frequency low. In addition, when the low-frequency trapezoidal wave i_0 is used, the v_0 is mainly determined by the resistance $R_a + 3R_z$ and the i_0 regardless of the rotating speed. In this article, the maximum v_0 due to the resistance component is 19.2 V. Therefore, the v_0 has little effect on the voltage utilization rate because the v_0 is sufficiently smaller than the maximum voltage norm of around 171 V that PWM inverter with the $V_{\rm dc}$ of 280 V can supply.

Unlike conventional adjustable field PMSM drive, the switching loss of inverter switch devices is almost the same as the standard PMSM drive because the switching device counts and the switching frequency are the same. In addition, copper loss and volume can be reduced since the proposed drive system has fewer wires than the conventional adjustable field PMSM drive system shown in Fig. 9(a) and (b).

As described previously, in addition to the i_d and the i_q, the proposed drive can control the i_0, and the i_0 can be used for the magnetic field control. Besides, the switching loss and the drive system volume are not sacrificed.

IV. Zero-Sequence Current for Field Control

A. Switching Time of Trapezoidal Wave Zero-Sequence Current

As described previously, the proposed drive system can not supply the dc i_0, and the trapezoidal wave i_0 is used for the magnetic field control. When the trapezoidal wave i_0 is supplied, iron loss occurs. Most of the iron loss occurs when the polarity of the i_0 changes because the frequency is very low. Therefore, in this section, the proper i_0 polarity switching time is determined based on the analysis results of the iron loss.

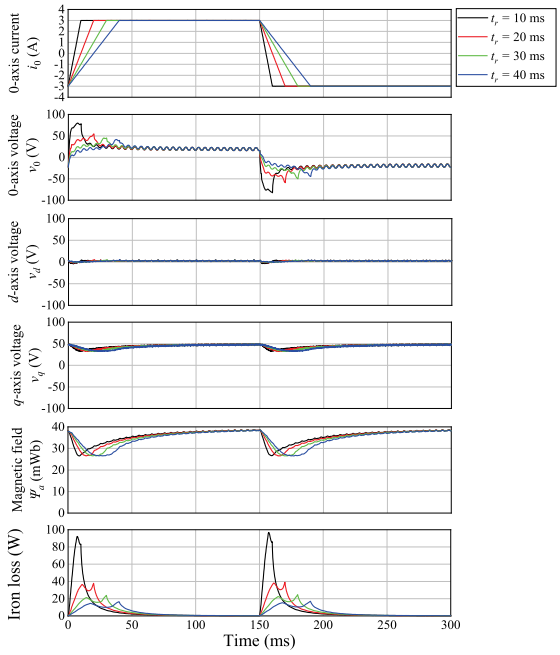

Fig. 11. Relationship between switching time of *0*-axis current polarity and operation characteristics of magnetic field control.

Fig. 11 shows the analysis results of the iron loss when the switching time t_r is changed from 10 ms to 40 ms. The period of the trapezoidal wave i_0 is unified to 300 ms. In this article, only the eddy current loss is calculated as the iron loss because there is no data about the hysteresis loop of the magnetic material SUS403 and SS400 and the PM S42SH in JMAG- designer. As shown in Fig. 11, the *0*-axis voltage v_0 increases instantaneously when the t_r is shorter. The v_0 surge causes temporary overmodulation. Therefore, a long t_r is necessary to avoid overmodulation.

$$\mathbf{i}_{0dq} = \boldsymbol{C}\mathbf{i}_{uvw}$$
$$\begin{bmatrix} i_0 \\ i_d \\ i_q \end{bmatrix} = \sqrt{\frac{2}{3}} \begin{bmatrix} i_z/\sqrt{2} \\ {i_u}' \cos\theta + {i_v}' \cos(\theta - 2\pi/3) + {i_w}' \cos(\theta + 2\pi/3) \\ -{i_u}' \sin\theta - {i_v}' \sin(\theta - 2\pi/3) - {i_w}' \sin(\theta + 2\pi/3) \end{bmatrix} \tag{5}$$

$$\mathbf{v}_{uvw} = R_a\mathbf{i}_{uvw} + \mathrm{p}\left(\mathbf{L}_{uvw}\mathbf{i}_{uvw}\right) + \mathrm{p}\boldsymbol{\Psi}_{uvw} + \mathbf{v}_z \text{ ; hence,}$$
$$\begin{bmatrix} v_u \\ v_v \\ v_w \end{bmatrix} = R_a \begin{bmatrix} i'_u + i_z/3 \\ i'_v + i_z/3 \\ i'_w + i_z/3 \end{bmatrix} + \mathrm{p}\left(\begin{bmatrix} L_u & M_{uv} & M_{wu} \\ M_{uv} & L_v & M_{vw} \\ M_{wu} & M_{vw} & L_w \end{bmatrix} \begin{bmatrix} i'_u + i_z/3 \\ i'_v + i_z/3 \\ i'_w + i_z/3 \end{bmatrix} \right)$$
$$+\mathrm{p} \begin{bmatrix} \Psi_{f1}(i_m)\cos\omega t + \Psi_{f3}(i_m)\cos 3\omega t \\ \Psi_{f1}(i_m)\cos(\omega t - 2\pi/3) + \Psi_{f3}(i_m)\cos 3(\omega t - 2\pi/3) \\ \Psi_{f1}(i_m)\cos(\omega t + 2\pi/3) + \Psi_{f3}(i_m)\cos 3(\omega t + 2\pi/3) \end{bmatrix}$$
$$+ \begin{bmatrix} R_z i_z + L_z \mathrm{p} i_z \\ R_z i_z + L_z \mathrm{p} i_z \\ R_z i_z + L_z \mathrm{p} i_z \end{bmatrix} \tag{7}$$

TABLE II
EXAMINATION RESULT OF SWITCHING TIME OF ZERO-SEQUECE CURRENT

	t_r = 10 ms	t_r = 20 ms	t_r = 30 ms	t_r = 40 ms
Current norm I_a	2.93 A_{rms}	2.86 A_{rms}	2.79 A_{rms}	2.72 A_{rms}
Maximum voltage norm V_{o_max}	89.1 V	69.0 V	62.7 V	58.9 V
Average magnetic field Ψ_{a_ave}	35.6 mWb	35.4 mWb	35.1 mWb	34.6 mWb
Copper loss P_{copper}	54.8 W	52.2 W	49.7 W	47.2 W
Iron loss P_{iron}	7.84 W	5.91 W	4.89 W	4.21 W

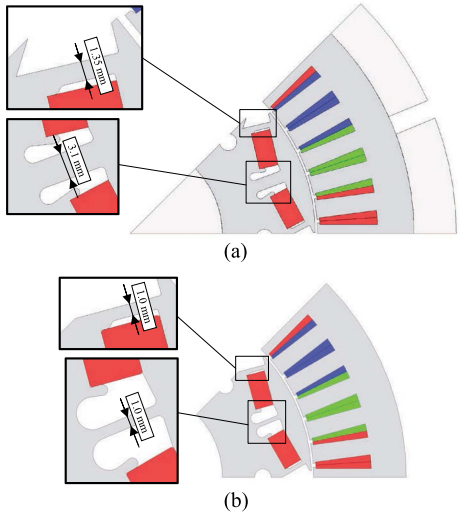

Fig. 12. Compared analysis models. (a) Protype motor model. (b) Standard IPMSM model. .

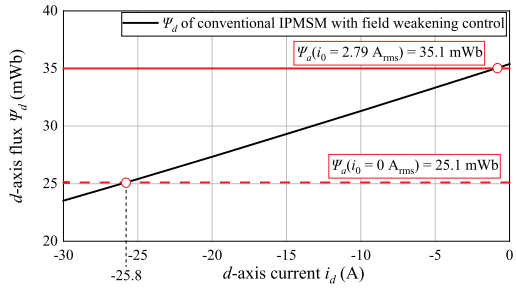

Fig. 13. Relationship between *d*-axis flux and *d*-axis current of standard IPMSM with field weakening control.

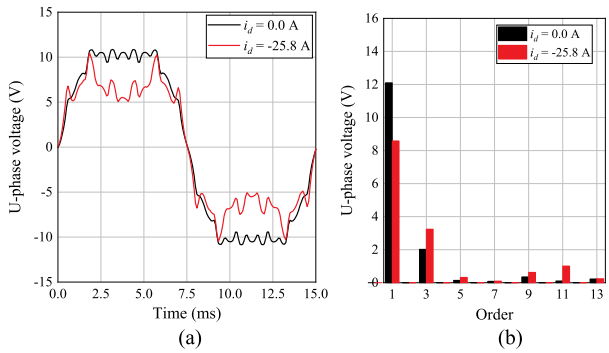

Fig. 14. U-phase voltage of standard IPMSM with field weakening control. (a) Waveforms. (b) FFT results.

Table II shows a summary of the article. From Table II, it can be seen that the current, voltage, copper loss, and iron loss can be reduced by setting the long t_r. However, the relationship between these evaluation items and the magnetic field amount Ψ_{a_ave} is a tradeoff. Therefore, the t_r is set to 30 ms in this article.

Next, in order to clarify the usefulness of the adjustable field control using trapezoidal wave i_0, the adjustable field control is compared with the traditional field weakening control based on the analysis result shown in Table II.

Fig. 12 shows compared analysis models. As shown in Fig. 12(a), the magnetic leakage paths of the prototyoe model have a width of 3.1 mm or 1.35 mm to enable field control. On the other hand, since a standard IPMSM does not require a wide-width bridge, the bridge width in Fig. 12(b) is set to 1.0 mm while considering mechanical strength. For a fair comparison, both motors have the same material, stator geometry, core stack length, number of armature winding turns, and PM volume.

Fig. 13 shows the relationship between the *d*-axis current i_d and the *d*-axis flux Ψ_d of the standard IPMSM with the field weakening control. The maximum Ψ_d is 35.4 mWb, which is almost the same as the Ψ_{a_ave} of the prototype motor with the trapezoidal wave i_0 of 2.79 A_{rms}, as shown in Table II. On the other hand, the i_d of -25.8 A is required to weaken the Ψ_d to the same level as the Ψ_{a_ave} of the prototype motor without the i_0.

Fig. 14 shows the analysis results of the U-phase voltage when the field weakening control is applied to the standard IPMSM. The rotating speed N is 1000 r/min, the same condition as the no-load experimental test in Section II. Therefore, the analysis results shown in Fig. 14 can be compared with the experimental result of the prototype motor shown in Fig. 7. As can be seen in Figs. 7 and 14, when the field weakening control is performed, the standard IPMSM generates much larger odd number harmonics such as 3rd, 5th, 9th, and 11th of the phase voltage than the prototype motor.

Table III shows the comparison results between the proposed adjustable field control and the traditional field weakening control. There is a significant difference between these control methods. In the field weakening control, the i_d is not supplied when the N is low, and the i_d to weaken the Ψ_d increases as the N increases. On the other hand, in the proposed adjustable field control, to output high torque during low-speed operation, the trapezoidal wave i_0 is given to increase the Ψ_a. Therefore, a performance comparison is conducted at the low-speed operating point ($N = 3000$ r/min) and the high-speed operating point ($N = 9000$ r/min). As shown in Table III, the proposed adjustable field control requires the current norm I_a of 2.79 A_{rms} to increase the Ψ_a of 10.0 mWb, resulting in the copper loss P_{copper} of 46.5 W. On the other hand, when the approximately equivalent amount of the Ψ_d is weakened by the field weakening control,

TABLE III
COMPARISON RESULT BETWEEN PROPOSED ADJUSTABLE FIELD CONTROL AND CONVENTIONAL FIELD WEAKENING CONTROL

Control method		Adjustable field	Field weakening
Low speed operating point (N = 3,000 r/min)	I_a	2.79 A_{rms}	0.00 A_{rms}
	$V_{o\ max}$	62.7 V	47.9 V
	Ψ_{a_ave} or Ψ_d	Ψ_{a_ave} = 35.1 mWb	Ψ_d = 35.4 mWb
	P_{copper}	49.7 W	0.00 W
	P_{iron}	4.89 W	0.01 W
High speed operating point (N = 9,000 r/min)	I_a	0.00 A_{rms}	25.8 A_{rms}
	$V_{o\ max}$	102 V	116 V
	Ψ_{a_ave} or Ψ_d	Ψ_{a_ave} = 25.1 mWb	Ψ_d = 25.1 mWb
	P_{copper}	0.00 W	56.6 W
	P_{iron}	43.0 W	96.4 W

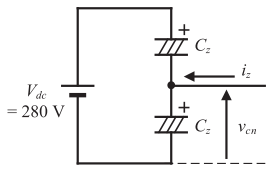

Fig. 15. Capacitor voltage.

the I_a of 25.8 A_{rms} is required, and the P_{copper} of 56.6 W is generated. In the low-speed range, since the v_0 increases instantaneously during the t_r, the maximum voltage norm V_{a_max} of the proposed adjustable field control is larger. On the other hand, the proposed adjustable field control does not require the i_0 in the high-speed range, whereas the conventional field weakening control supplies the large i_d. Therefore, the V_{a_max} and the iron loss P_{iron} of the conventional field weakening control is larger because more significant harmonics are caused by the field weakening control, as can be seen in Figs. 7 and 14.

B. Smoothing Capacitor

As illustrated in Fig. 11, iron loss occurs during the switching time t_r of the i_z polarity. Therefore, the iron loss caused by the field control can be reduced by setting a long trapezoidal wave period T_z. However, there is a tradeoff relationship between the T_z and C_z. The C_z is usually determined by the capacity of the inverter or motor. The C_z is set to 6600 μF in this article. Based on the C_z, the T_z is calculated in this section.

Fig. 15 shows the capacitor voltage v_{cn}, and Fig. 16 shows the waveforms of the i_z and the v_{cn}. The v_{cn} change is expressed as

$$v_{cn}(t) = \frac{1}{2C_z}\int i_z dt + v_{cn}(0) = \frac{1}{2C_z}\int i_z dt + 0.4\mathrm{V_{dc}}. \tag{9}$$

In this article, since the i_z is supplied while controlling the v_{cn} in the range of 0.4 V_{dc} to 0.6 V_{dc}, the v_{cn} becomes 0.6 V_{dc} after the positive period of the i_z shown in the red area in Fig. 16 is completed as the following equation:

$$v_{cn}(0.5T_z) = \frac{1}{4C_z}(T_z - t_r) I_{z\_amp} + 0.4\mathrm{V_{dc}} = 0.6\mathrm{V_{dc}}. \tag{10}$$

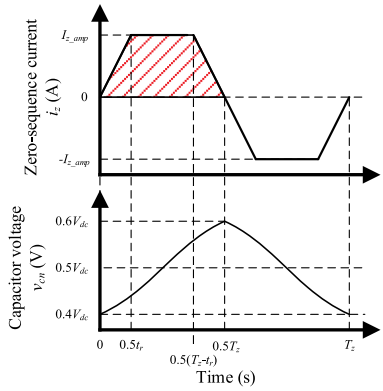

Fig. 16. Waveforms of v_{cn} and i_z.

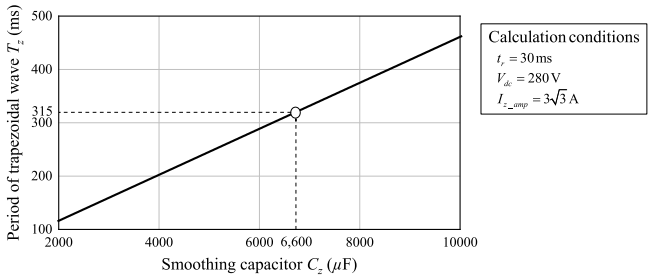

Fig. 17. Relationship between T_z and C_z.

By solving (10) for the T_z, the relationship between the T_z and C_z can be derived as

$$T_z = \frac{0.8\mathrm{V_{dc}}C_z}{I_{z\_amp}} + t_r. \tag{11}$$

Fig. 17 shows the relationship between the T_z and C_z obtained from (11) when the t_r is 30 ms, the dc-bus voltage V_{dc} is 280 V, and the trapezoidal wave i_z amplitude I_{z_amp} is $3\sqrt{3}$A. From Fig. 17, the T_z is expected to be 315 ms when the C_z is 6600 μF.

C. Experimental Test of 0DQ Current Control

The control block diagram of the prototype motor is shown in Fig. 18. The control block is designed based on (8), and dead time t_d is compensated based on [23]–[27]. Fig. 19 shows a photograph of the proposed drive system. Three current sensors for each line current are needed when the i_z is controlled. Therefore, there are three current sensors in the proposed drive system.

In Section III, the mathematical model of the prototype motor is derived, as shown in Eq. (8). However, in fact, the midpoint of the dc-bus voltage fluctuates due to the charge and discharge of the smoothing capacitor. Thus, it is necessary to consider the capacitance C_z for the i_z control. The *0*-axis voltage $v_0(t)$ when the C_z is taken into consideration can be expressed as follows using the *0*-axis current $i_0(t)$:

$$v_0(t) = (R_a + 3R_z) i_0(t) + 3L_z \frac{\mathrm{d}}{\mathrm{d}t} i_0(t) + \frac{3}{2C_z}\int i_0(t)\,\mathrm{d}t. \tag{12}$$

By Laplace transforming (12) and solving for the i_0, the plant's transfer function $P_0(s)$ can be derived, as shown in the

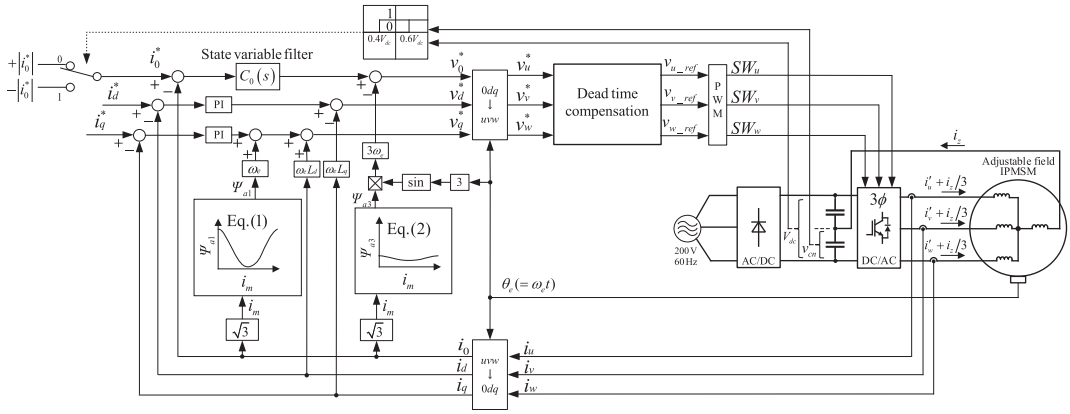

Fig. 18. Control block diagram of prototype motor.

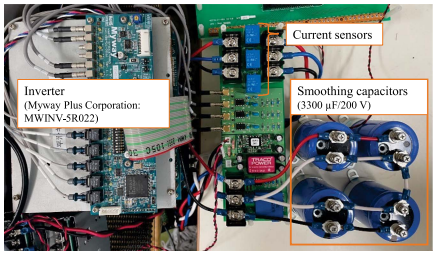

Fig. 19. Photograph of proposed drive.

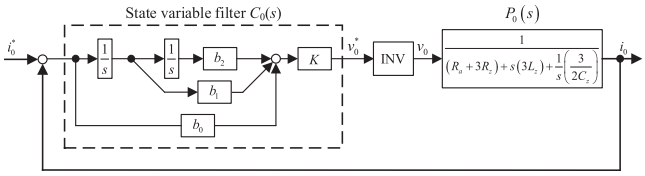

Fig. 20. SVF for *0*-axis current control.

following equation:

$$i_0(s) = \frac{v_0(s)}{(R_a + 3R_z) + s(3L_z) + \frac{1}{s}\left(\frac{3}{2C_z}\right)} = P_0(s)\, v_0(s). \tag{13}$$

As expressed in (13), the order of the plant is quadratic. Therefore, the i_0 is controlled using a two-stage state variable filter (SVF) $C_0(s)$, as shown in Fig. 20. From this figure, the open-loop transfer function $G_0(s)$ is expressed as

$$G_0(s) = C_0(s)\, P_0(s) = \left(K\frac{b_0 s^2 + b_1 s + b_2}{s^2}\right) \times \left(\frac{1}{(R_a + 3R_z) + s(3L_z) + \frac{1}{s}\left(\frac{3}{2C_z}\right)}\right). \tag{14}$$

Based on (14), the i_0 control system can be made into a first-order lag system by setting each SVF constant as follows:

$$(K, b_0, b_1, b_2) = \left(3\omega_c L_z, 1, \frac{R_a + 3R_z}{3L_z}, \frac{1}{2C_z L_z}\right). \tag{15}$$

TABLE IV
EXPERIMENTAL CONDITIONS OF 0DQ CURRENT CONTROL

Parameter	Symbol	Value
DC-bus voltage	V_{dc}	280 V
Switching frequency	f_{sw}	20 kHz
Dead time	t_d	4 μs
Modulation winding resistance	R_z	2.1 Ω
Armature winding resistance	R_a	0.085 Ω
Modulation winding inductance	L_z	60 mH
d-axis inductance	L_d	1.0 mH
q-axis inductance	L_q	1.6 mH
Smoothing capacitor	C_z	6,600 μF
Crossover frequency	ω_c	3,000 rad/s

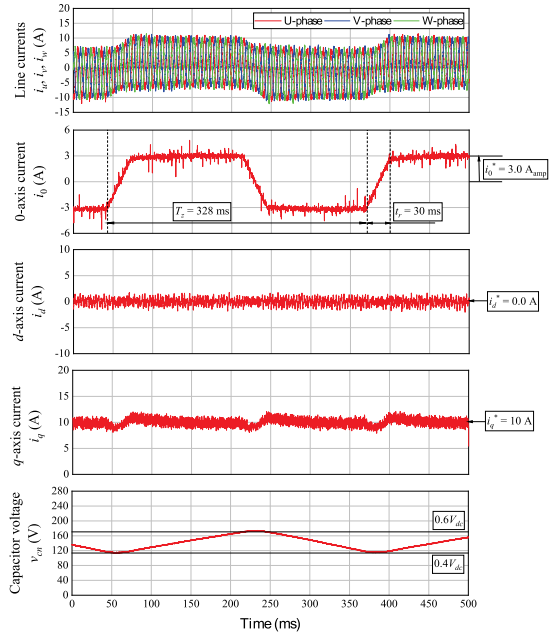

Fig. 21. Waveforms of 0dq current control using SVF.

Next, the experiment of the 0*dq* current control is carried out to verify the validity of the control block diagram. Table IV shows the experimental test conditions of 0*dq* current control. Fig. 21 shows the experimental result of the 0*dq* current control. It can be confirmed that the 0-, *d*-, and *q*-axis currents can be controlled independently. In addition, the T_z is 328 ms, which is

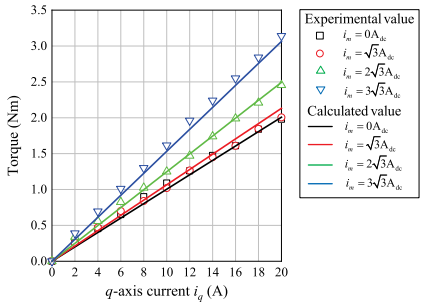

Fig. 22. I-T characteristic of prototype motor.

TABLE V
AVERAGE TORQUE RESULT WITH TORQUE COMMAND VALUE OF 2 NM

	Without compensation	With compensation
Average torque	1.68 Nm	1.97 Nm

almost the same as the calculated value shown in Fig. 17. Furthermore, the v_{cn} can be controlled within the range of 0.4 V_{dc} to 0.6 V_{dc}.

V. TORQUE DROP COMPENSATION DURING ALTERNATION OF ZERO-SEQUENCE CURRENT POLARITY

The prototype motor is a reverse salient pole IPMSM, so reluctance torque can be delivered. However, the i_d is not used to avoid complicating verification in this article. Therefore, the torque T of the prototype motor is expressed as

$$T = P_n \Psi_a (i_m) i_q \tag{16}$$

where P_n is the pole pair.

An experiment of the relationship between the q-axis current i_q and the T (I-T characteristics) is conducted to validate (16). The experimental result is shown in Fig. 22. However, in order to evaluate the torque characteristic of the motor hardware alone, the dc i_m is supplied directly to the modulation winding using an additional dc power supply prepared separately from the three-phase inverter. As can be seen in Fig. 22, the torque model expressed in (16) corresponds reasonably well with the experimental value. In other words, the prototype motor can output the higher torque with the small i_q because the Ψ_a becomes large by applying the i_m.

On the other hand, when the trapezoidal wave i_0 is utilized as the i_m, the Ψ_a is reduced during the switching time t_r of the i_0 polarity. When the Ψ_a decreases, the torque also decreases based on the torque model, so it is necessary to compensate with the i_q. Fig. 23 and Table V show the waveforms of the 0dq currents and the torque result, respectively. The torque command $T*$ is 2.0 Nm. In addition, the t_r is intentionally set to 300 ms in this experiment to emphasize the i_q change and the compensation effect. When the i_q compensates for the torque drop during the t_r, the q-axis current command value i_q* is determined by (16). Therefore, as shown in Fig. 23(b), the i_q increases during the t_r. In addition, the T reaches the $T*$ due to the torque drop compensation, as shown in Table V.

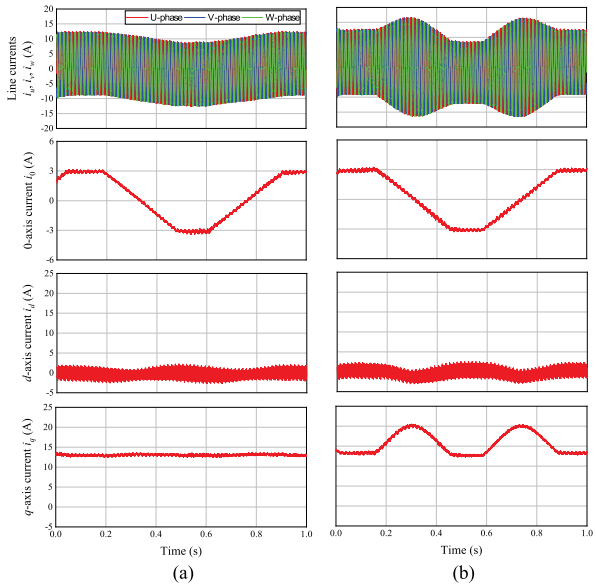

Fig. 23. 0dq current waveforms. (a) Without torque drop compensation. (b) With torque drop compensation.

VI. COMPARISON OF OPERATION CHARACTERISTICS AMONG THREE PROPOSED DRIVES

A. FEM Analysis

The previous sections examined the three-phase four-wire inverter drive system that uses zero-sequence current i_z for field control. However, from (1), it is sufficient to supply the i_m with a constant absolute value to output a stable torque. Therefore, the drive systems that can be applied as the prototype motor drive system are as follows, as shown in Fig. 1:

1) A system using a dc power supply and a three-phase three-wire inverter (Compared drive system A).
2) A system using a single-phase inverter and a three-phase three-wire inverter (Compared drive system B).
3) Proposed system using a three-phase four-wire inverter.

Table VI shows comparison results among three drive systems. Five wires need to be wired to the prototype motor in the system that uses additional circuits such as a dc power supply or a single-phase inverter. On the other hand, there are four wires in the proposed drive system. Therefore, the copper volume can be reduced. In addition, the number of switching devices in the proposed drive system is smaller than the other compared drive systems. Thus, the switching losses can be improved.

Next, the torque analysis results with torque command $T*$ of 2 Nm shown in Table VI are discussed. The difference between the compared drive systems A and B are whether the i_m is dc or trapezoidal. As shown in Table VI, the torque T with trapezoidal wave i_m deteriorates by 5.5% because the iron loss P_{iron} increases due to trapezoidal wave i_m. The difference between the compared drive system B and the proposed drive system is whether the i_m flows through the armature windings. Due to the difference, the copper loss P_{copper} and line current of the proposed system is slightly higher than that of the compared drive system B. On the other hand, it can be seen from Table VI

TABLE VI
COMPARISON OF DRIVE SYSTEM

Drive system			Compared drive system A	Compared drive system B	Proposed drive system
Circuit specifications	Modulation current		DC i_m of $3\sqrt{3}$ A_{dc}	Trapezoidal wave i_m of $3\sqrt{3}$ A_{amp}	Trapezoidal wave i_0 of $3A_{amp}$
	Number of wires		5	5	4
	Number of switch devices		More than 8	More than 8	6
Analysis result with T^* of 2 Nm	Loss	P_{copper}	57.7 W	50.9 W	51.0 W
		P_{iron}	0.12 W	4.54 W	4.54 W
	Output	N	1,500 r/min	1,500 r/min	1,500 r/min
		T	2.00 Nm	1.89 Nm	1.89 Nm

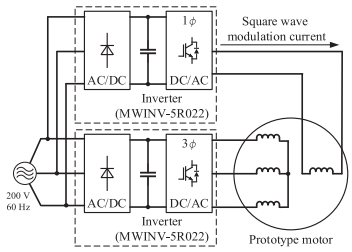

Fig. 24. Experimental circuit of compared drive system B.

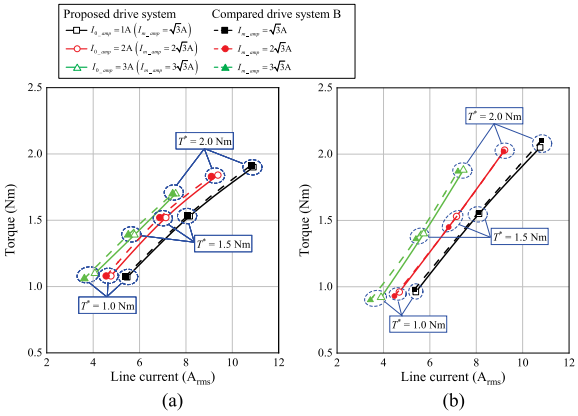

Fig. 25. I-T characteristics of prototype motor with trapezoidal wave i_m. (a) $N = 1500$ r/min. (b) $N = 3000$ r/min.

that even if the i_m flows through the armature winding, it does not affect the T and P_{iron}.

B. Experimental Test

In the previous section, it was found through the FEM analysis that even if the i_z flows through the armature winding, there is no effect on the torque output. In this section, the I-T characteristic of the prototype motor is measured using the compared drive system B and the proposed drive system to verify the validity and usefulness in more detail. Fig. 24 shows the experimental circuit of the compared drive system B. The inverter of the compared drive system B is MWINV-5R022, Myway Plus Corporation, which is the same as the proposed drive system.

Fig. 25 shows the experimental results of the I-T characteristics with the $T*$ of 1.0 Nm, 1.5 Nm, or 2.0 Nm. From the results shown in Fig. 25, three things can be confirmed. First, the prototype motor can deliver high torque with a small line current by supplying the trapezoidal wave i_0. Second, torque deterioration is improved as the N increases. As described in Section VI-A, the torque deteriorates due to iron loss when the trapezoidal wave i_m is used. However, the iron loss is constant regardless of the N because the smoothing capacitor C_z determines the frequency of the trapezoidal wave i_m, as discussed in Section IV-B. In other words, the effect of the iron loss caused by the trapezoidal wave i_m becomes relatively tiny as the N increases, so torque deterioration is improved. And finally, a comparison between the compared drive system B and the proposed drive system shows that the proposed drive requires a larger line current due to the flow of the i_z, but the difference is negligibly slight.

VII. CONCLUSION

This article described a three-phase four-wire inverter fed adjustable field IPMSM drive utilizing magnetic saturation.

In Section II, through the no-load e.m.f. measurement test, it was found that the magnetic field of the prototype motor can be widely adjusted depending on the absolute value of the i_m.

Section III compares the proposed drive system with the conventional adjustable field PMSM drives. As a comparison results, the following merits were revealed:

1) The proposed drive system has good controllability that can continuously and actively control the field.
2) The proposed simple drive system does not require a large-capacity inverter or additional circuit.

In Section IV, the proper i_z waveform was determined from the viewpoint of iron loss and the capacitance of the smoothing capacitor. In addition, the proposed adjustable field control and the traditional field weakening control were compared. The advantages of the proposed adjustable field control are as follows:

1) The current norm is 89.2% smaller, and the copper loss is 12.2% smaller under conditions that control around the same amount of the Ψ_a or Ψ_d, as shown in Table III.
2) Figs. 7 and 14 show that all odd-order voltage harmonics are smaller.
3) As can be seen in Table III, iron loss by 55.4% can be reduced at the high-speed operating point with a rotating speed of 9000 r/min.

In Section V, the validity of the torque model of the prototype motor was examined using a dc power supply, and the torque drop compensation during the switching time of the trapezoidal wave i_z polarity was investigated based on the torque model.

In Section VI, the proposed drive system was compared with the compared drive systems using an additional circuit, and the following contributions were clarified:

1) The wiring to the motor can be reduced by one.
2) At least two switching devices can be reduced.

3) The same torque as when using an additional single-phase inverter can be delivered even without additional circuits.

The conventional vector control algorithms such as MTPA control and MTPV control are established in the *dq* reference frame. However, the mathematical model of the prototype motor and the proposed drive system is represented by the 0*dq* reference frame, as expressed in (8). Therefore, the authors will consider the control that extends the conventional control expressed in the *dq* reference frame to the 0*dq* reference frame as future work.

References

[1] T. Sun and J. Wang, "Extension of virtual-signal-injection-based MTPA control for interior permanent-magnet synchronous machine drives into the field-weakening region," *IEEE Trans. Ind. Electron.*, vol. 62, no. 11, pp. 6809–6817, Nov. 2015.

[2] X. Zhang, G. H. B. Foo, and M. F. Rahman, "A robust field-weakening approach for direct torque and flux controlled reluctance synchronous motors with extended constant power speed region," *IEEE Trans. Ind. Electron.*, vol. 67, no. 3, pp. 1813–1823, Mar. 2020.

[3] S. Y. Jung, C. C. Mi, and K. Nam, "Torque control of IPMSM in the field-weakening region with improved DC-link voltage utilization," *IEEE Trans. Ind. Electron.*, vol. 62, no. 6, pp. 3380–3387, Jun. 2015.

[4] S. Chaithongsuk, B. Nahid-Mobarakeh, J. P. Caron, N. Takorabet, and F. Meibody-Tabar, "Optimal design of permanent magnet motors to improve field-weakening performances in variable speed drives," *IEEE Trans. Ind. Electron.*, vol. 59, no. 6, pp. 2484–2494, Jun. 2012.

[5] J. Liu, C. Gong, Z. Han, and H. Yu, "IPMSM model predictive control in flux-weakening operation using an improved algorithm," *IEEE Trans. Ind. Electron.*, vol. 65, no. 12, pp. 9378–9387, Dec. 2018.

[6] J. A. Tapia, F. Leonardi, and T. A. Lipo, "Consequent-pole permanent-magnet machine with extended field-weakening capability," *IEEE Trans. Ind. Appl.*, vol. 39, no. 6, pp. 1704–1709, Jun. 2003.

[7] T. Mizuno, K. Nagayama, T. Ashikaga, and T. Kobayashi, "Basic principles and characteristics of hybrid excitation type synchronous machine," *IEEJ Trans. Ind. Appl.*, vol. 115, no. 11, pp. 1402–1411, Nov. 1995.

[8] K. Sakai, H. Hashimoto, and S. Kuramochi, "Principle and basic characteristics of variable-magnetic-force memory motors," in *Proc. IEEJ Trans. Ind. Appl.*, 2011, pp. 53–60.

[9] J. Chen, J. Li, and R. Qu, "Maximum-torque-per-ampere and magnetization-state control of a variable-flux permanent magnet machine," *IEEE Trans. Ind. Electron.,* vol. 65, no. 2, pp. 1158–1169, Feb. 2018.

[10] X. Zhu, Z. Xiang, L. Quan, W. Wu, and Y. Du, "Multimode optimization design methodology for a flux-controllable stator permanent magnet memory motor considering driving cycles," *IEEE Trans. Ind. Electron.*, vol. 65, no. 7, pp. 5353–5366, Jul. 2018.

[11] M. Aoyama and T. Noguchi, "Automatic variable magnetic flux technique in consequent pole type PM-motor utilizing space harmonic," in *Proc. Int. Symp. Power Electron., Elect. Drives, Automat. Motion*, 2018, pp. 1315–1320.

[12] H. Hijikata, Y. Sakai, K. Akatsu, Y. Miyama, H. Arita, and A. Daikoku, "Multi-phase inverter-fed MATRIX motor for high efficiency driving," *IEEJ Trans. Ind. Appl.*, vol. 138, no. 3, pp. 257–264, Mar. 2018.

[13] K. Iwama and T. Noguchi, "Operation characteristics of adjustable field IPMSM utilizing magnetic saturation," *Energies*, vol. 15, no. 1, p. 52, 2021, doi: 10.3390/en15010052.

[14] M. Narimani and G. Moschopoulos, "An investigation on the novel use of high-power three-level converter topologies to improve light-load efficiency in low power DC/DC full-bridge converters," *IEEE Trans. Ind. Electron.*, vol. 61, no. 10, pp. 5690–5692, Oct. 2014.

[15] M. Das and V. Agarwal, "Design and analysis of a high-efficiency DC-DC converter with soft switching capability for renewable energy applications requiring high voltage gain," *IEEE Trans. Ind. Electron.*, vol. 63, no. 5, pp. 2936–2944, May 2016.

[16] A. Mondzik, R. Stala, S. Pirog, A. Penczek, P. Gucwa, and M. Szarek, "High efficiency DC-DC boost converter with passive snubber and reduced switching losses," *IEEE Trans. Ind. Electron.*, , vol. 69, no. 3, pp. 2500–2510, Mar. 2022.

[17] K. Dang *et al.*, "Lateral GaN Schottky barrier diode for wireless high-power transfer application with high RF/DC conversion efficiency: From circuit construction and device technologies to system demonstration," *IEEE Trans. Ind. Electron.*, vol. 67, no. 8, pp. 6597–6606, Aug. 2020.

[18] P. Nayak and K. Hatua, "Parasitic inductance and capacitance-assisted active gate driving technique to minimize switching loss of SiC MOSFET," *IEEE Trans. Ind. Electron.*, vol. 64, no. 10, pp. 8288–8298, Oct. 2017.

[19] X. Li *et al.*, "A SiC power MOSFET loss model suitable for high-frequency applications," *IEEE Trans. Ind. Electron.*, vol. 64, no. 10, pp. 8268–8276, Oct. 2017.

[20] A. P. Camacho, V. Sala, H. Ghorbani, and J. L. R. Martinez, "A novel active gate driver for improving SiC MOSFET switching trajectory," *IEEE Trans. Ind. Electron.*, vol. 64, no. 11, pp. 9032–9042, Nov. 2017.

[21] M. R. Ahmed, R. Todd, and A. J. Forsyth, "Predicting SiC MOSFET behavior under hard-switching, soft-switching, and false turn-on conditions," *IEEE Trans. Ind. Electron.*, vol. 64, no. 11, pp. 9001–9011, Nov. 2017.

[22] Y. Fujii, J. Asama, and A. Chiba, "Voltage sensorless control of split capacitor for three-phase four-wire motor system with zero-sequence suspension winding," *IEEE Trans. Ind. Appl.*, vol. 57, no. 6, pp. 6823–6832, Nov./Dec. 2021.

[23] Y. Oto, T. Noguchi, T. Sasaya, T. Yamada, and R. Kazaoka, "Space vector modulation of dual-inverter system focusing on improvement of multilevel voltage waveforms," *IEEE Trans. Ind. Electron.*, vol. 66, no. 12, pp. 9139–9148, Dec. 2019.

[24] Y. Wang, Q. Gao, and X. Cai, "Mixed PWM for dead-time elimination and compensation in a grid-tied inverter," *IEEE Trans. Ind. Electron.*, vol. 58, no. 10, pp. 4797–4803, Oct. 2011.

[25] D. M. Park and K. H. Kim, "Parameter-independent online compensation scheme for dead time and inverter nonlinearity in ipmsm drive through waveform analysis," *IEEE Trans. Ind. Electron.*, vol. 61, no. 2, pp. 701–707, Feb. 2014.

[26] G. Liu, D. Wang, Y. Jin, M. Wang, and P. Zhang, "Current-detection-independent dead-time compensation method based on terminal voltage A/D conversion for PWM VSI," *IEEE Trans. Ind. Electron.*, vol. 64, no. 10, pp. 7689–7699, Oct. 2017.

[27] U. Abronzini, C. Attaianese, M. D'Arpino, M. Di Monaco, and G. Tomasso, "Steady-state dead-time compensation in VSI," *IEEE Trans. Ind. Electron.*, vol. 63, no. 9, pp. 5858–5866, Sep. 2016.

Kiyohiro Iwama (Student Member, IEEE) was born in Fuji, Japan, in 1995. He received the B.Eng. and M.Eng. degrees in 2018 and 2020, respectively, from Shizuoka University, Hamamatsu, Japan, where he is currently working toward the Ph.D. degree with the Department of Environment and Energy System, Graduate School of Science and Technology.

His research subject since he was an undergraduate has been motor hardware of an adjustable field PMSM and its drive system.

Mr. Iwama is a student member of the Institute of Electrical and Electronics Engineers (IEEE) and the Institute of Electrical Engineers of Japan (IEEJ).

Toshihiko Noguchi (Senior Member, IEEE) was born in Kuwana, Japan, in 1959. He received the B.Eng. degree in electrical engineering from the Nagoya Institute of Technology, Nagoya, Japan, in 1982, and the M.Eng. and D.Eng. degrees in electrical and electronics systems engineering from the Nagaoka University of Technology, Nagaoka, Japan, in 1986 and 1996, respectively.

In 1982, he was with the Toshiba Corporation, Tokyo, Japan. He was a Lecturer with the Gifu National College of Technology, Gifu, Japan, from 1991 to 1993. He was an Assistant Professor and an Associate Professor with the Department of Electrical, Electronics and Information Engineering, Nagaoka University of Technology, from 1994 to 1995 and from 1995 to 2009, respectively. Since 2009, he has been a Professor with the Department of Electrical and Electronics Engineering, Faculty of Engineering, Graduate School of Engineering, Shizuoka University, Hamamatsu, Japan. His research interests include new circuit topologies of static power converters and motor drives including electric machine hardware.

Mr. Noguchi is a Member of the Institute of Electrical Engineers of Japan.